

## The crystal structure of diopside at pressure to 10 GPa

RICHARD M. THOMPSON\* AND ROBERT T. DOWNS

Department of Geosciences, University of Arizona, Tucson, Arizona, 85721-0077, U.S.A.

### ABSTRACT

The crystal structure of diopside has been determined at various pressures to 10.16 GPa. The results to 5 GPa are consistent with Levien and Prewitt (1981). The crystal structures have been analyzed using the geometric pyroxene model of Thompson and Downs (2004), the anion packing algorithm of Thompson and Downs (2001), and a new algorithm that quantifies the distortion of observed pyroxenes from their geometric model equivalents. Diopside is shown to compress via three main mechanisms: isotropic scaling, kinking of the tetrahedral chains, and collapse of the M1 chain toward its axis. The kinking of the chains accounts for most of the anisotropy of compression observed in the **a-c** plane, and the collapse of the M1 chain explains the anisotropy seen in the **b-c** plane. Model behavior is shown to reproduce many of the observations of previous workers. Anion-anion interactions are shown to be important in the distortion of observed diopside from its geometric model equivalent.

**Keywords:** Diopside, crystal structure, high-pressure, model pyroxene

### INTRODUCTION

The list of systematic single-crystal studies of the pyroxene structure as a function of pressure to date includes  $(\text{Ca}_{0.97}\text{Fe}_{0.02}\text{Mg}_{0.01})(\text{Mg}_{0.57}\text{Fe}_{0.21}\text{Al}_{0.16}\text{Ti}_{0.06})(\text{Si}_{1.72}\text{Al}_{0.28})\text{O}_6$  augite (Hazen and Finger 1977),  $\text{CaMgSi}_2\text{O}_6$  diopside (Levien and Prewitt 1981),  $\text{Mg}_2\text{Si}_2\text{O}_6$  enstatite (Hugh-Jones and Angel 1994),  $\text{Fe}_2\text{Si}_2\text{O}_6$  ferrosilite (Hugh-Jones et al. 1997),  $\text{CaFeSi}_2\text{O}_6$  hedenbergite (Zhang et al. 1997),  $\text{Mg}_{1.54}\text{Li}_{0.23}\text{Sc}_{0.23}\text{Si}_2\text{O}_6$  (Yang et al. 1999),  $\text{FeGeO}_3$  (Hattori et al. 2000),  $\text{NaCrSi}_2\text{O}_6$  kosmochlor (Origlieri et al. 2003),  $(\text{Mg}_{0.85}\text{Ca}_{0.15})\text{MgSi}_2\text{O}_6$  pigeonite (Nestola et al. 2004),  $(\text{Mg}_{0.93}\text{Ca}_{0.07})\text{MgSi}_2\text{O}_6$  enstatite (Nestola et al. 2006),  $(\text{Ca}_{0.88}\text{K}_{0.12})(\text{Mg}_{0.83}\text{Al}_{0.17})(\text{Si}_{1.98}\text{Al}_{0.02})\text{O}_6$  (Bindi et al. 2006),  $\text{NaAlSi}_2\text{O}_6$  jadeite (McCarthy et al. 2008), and the jadeite-hedenbergite join (Nestola et al. in prep.). In addition, there are several studies of the structures of pyroxenes at pressure in which the goals were to determine and characterize phase transitions. These studies were mainly concerned with obtaining cell parameters, but a small number of crystal structures at pressure have been reported, and these include the structures of  $\text{Fe}_2\text{Si}_2\text{O}_6$  clinoferrosilite (Hugh-Jones et al. 1994),  $\text{Mn}_{0.84}\text{Mg}_{1.16}\text{Si}_2\text{O}_6$  kanoite (Arlt et al. 1998),  $\text{LiAlSi}_2\text{O}_6$  spodumene,  $\text{LiScSi}_2\text{O}_6$ , and  $\text{ZnSiO}_3$  (Arlt and Angel 2000). A recent summary of the structural behavior of pyroxene at pressure can be found in Yang and Prewitt (2000).

Pyroxenes have also been characterized at high pressure using Raman spectroscopy (cf. Gatta et al. 2005; Pommier et al. 2003, 2005). Recently, Chopelas and Serghiou (2002) presented Raman spectroscopic evidence for pressure-induced phase transitions in diopside. They observed discontinuous changes in the spectra at 10, 15, and 55 GPa. They suggest that (1) at 10 GPa there is a  $C2/c$  to  $C2/c$  transition related to bonding changes around the

Ca atom in the M2 site; (2) at 15 GPa a change in compression mechanism takes place; and (3) at 55 GPa there is a change in the silicon coordination. A high-pressure  $C2/c$  phase has been observed in several different pyroxenes, for instance kanoite (Arlt et al. 1998) and  $\text{ZnSiO}_3$  (Arlt and Angel 2000) but in each case the  $C2/c$  phase was formed by a transformation from a structure with  $P2_1/c$  symmetry. Based upon crystal chemical systematics of pyroxenes, Downs et al. (1999) and Downs (2003) proposed that a  $C2/c$  to  $C2/c$  transition in diopside is possible, and Thompson and Downs (2002, 2004) modeled the transition pathway, but no structural study has yet demonstrated it.

This study follows up on the work of Levien and Prewitt (1981) who compressed diopside to the relatively low pressure of 5 GPa. Because of the pioneering nature of the Levien and Prewitt (1981) study some doubt has been expressed at various scientific meetings about the quality of its data. The present paper shows that while the Levien and Prewitt (1981) study has more scatter in its data than today's standards, the general trends indicated in their paper are valid and are reproduced.

The scientific purpose of this paper is to present experimental data to higher pressures than previously reported and to analyze the compressional systematics of diopside using a recently developed geometric model of the pyroxenes, described below, and to review the analyses of earlier works in the context of this model. Previous attempts to understand the atomic scale mechanism of compression in diopside have focused on the compression of the individual polyhedral units. Levien and Prewitt (1981) reported their surprise that the  $\text{MgO}_6$  octahedra were slightly more compressible than the  $\text{CaO}_8$  polyhedra. They suggested that the compression of the structure is not sensitive to composition, but is controlled by the directions and compressibilities of the bonds in the M1 and M2 polyhedra because the least compressed M-O bonds can be correlated with the direction of minimum compres-

\* E-mail: thompson@geo.arizona.edu

sion of the whole crystal, while the most compressible bonds, M2-O(3<sub>1</sub>,3<sub>4</sub>), are oriented 45° between the two most compressible principal axes of the strain ellipsoid (nomenclature after Downs 2003, see Fig. 1 this paper).

In their study of the structure of hedenbergite to 10 GPa, Zhang et al. (1997) also determined the cell parameters of diopside and characterized the axial compressibilities of the two phases. They reported that both diopside and hedenbergite exhibit anisotropic compression, with linear axial compressibility ratios of  $\beta_a:\beta_b:\beta_c = 1:1.34:1.06$  for diopside, and  $1:1.75:1.25$  for hedenbergite. They observed that the compressibility of the polyhedral units (7.3%) in hedenbergite is greater than that of the voids (6.7%) and concluded that the unit-cell volume compression is dependent upon the polyhedral compressibilities. The SiO<sub>4</sub> groups are quite incompressible, so they deduced that compression is dominated by the other cation polyhedra. Furthermore, since these pyroxenes are constructed of sheets of CaO<sub>8</sub> and (Fe,Mg)O<sub>6</sub> polyhedra alternating with sheets of SiO<sub>4</sub> groups, all stacked along *a*\*, it follows that there is only a small component of compression along the *a* axis. The bending of the Si-O-Si angles promotes compression along the *c* axis and the long Ca-O bonds projected onto the *b* axis account for the compressibility of the structure in the *b*-axis direction.

In a synchrotron X-ray powder diffraction study of diopside to 40 GPa, Tribaudino et al. (2000) observed a change in compression mechanism around 5–10 GPa. At lower pressures the behavior is dominated by compression along the *b* axis and at a direction 145° from the *c* axis in the (010) plane. At higher pressures, the behavior is dominated by compression along the *b* axis. They suggest that these two behaviors are related to shearing of the tetrahedral chains, which may reduce the volume of the M2 polyhedron and increase its regularity. Once the shearing has

progressed till the four M2-O3 bonds achieve similar lengths at between 5 and 10 GPa, then the compression mechanism of the pyroxene changes.

Hazen and Finger (1977) suggested that the anion skeleton of clinopyroxenes becomes more eutactic (i.e., close-packed) with pressure. Thompson and Downs (2001) quantified the degree to which observed pyroxene structures deviate from ideal closest-packed arrays of O atoms, and found that observed pyroxene structures systematically become more closest-packed with pressure. In their high-pressure structural study of kosmochlor, Origlieri et al. (2003) showed that the average M1-O and M2-O bond distances in pyroxenes do not correlate with the bulk modulus, and argued that the polyhedral volumes do not determine compression. Furthermore, they showed that the strain ellipsoids of several pyroxenes are oriented in directions that correspond to the stacking directions of the oxygen monolayers.

Thompson and Downs (2004) and Thompson et al. (2005) derived crystal structure data for hypothetical pyroxenes with ideal regular tetrahedra and M1 octahedra (Fig. 1), and modeled pyroxene behavior under changing conditions with these virtual crystals. These hypothetical constructs are hereafter referred to as model pyroxenes, and the scheme as a whole is referred to as the TD model. The model simplifies the pyroxene structure, and provides the means to focus on the important mechanisms that pyroxenes use to respond to changing conditions, i.e., isotropic scaling of the structure and kinking (or unkinking) of the tetrahedral chains. In observed pyroxenes, the distortion of M1 and T from perfectly regular is real, but minor. Comparing observed and model pyroxenes permits the separation of mechanisms so that they can be examined independently.

The crystal structure of a model pyroxene can be calculated from two parameters: the O3-O3-O3 angle,  $\theta$ , and the model

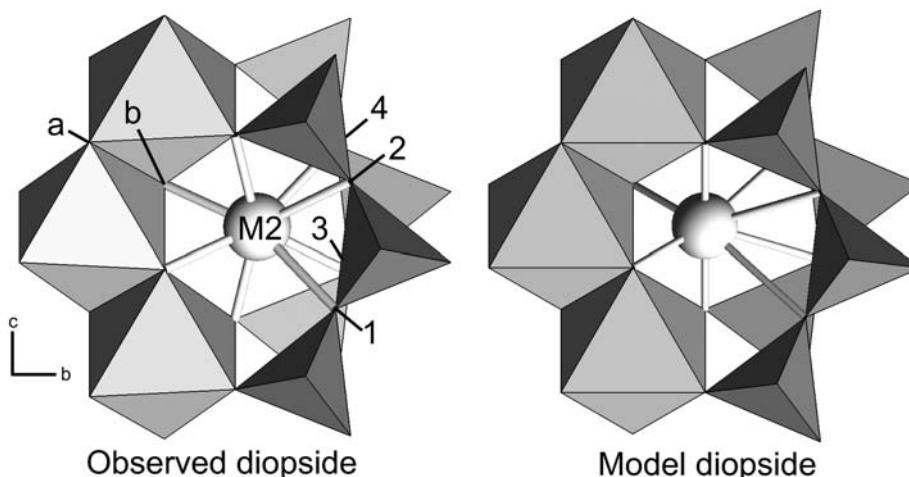


**FIGURE 1.** A comparison of observed and model diopside with nomenclature (after Downs 2003) used to discuss the bonding around M2. The model diopside has the same unit-cell volume and O3-O3-O3 angle,  $\theta$ , as observed diopside, but M1 and T are ideal regular polyhedra. The O3's that can be bonded to M2 are labeled O3<sub>1</sub>, O3<sub>2</sub>, O3<sub>3</sub>, and O3<sub>4</sub>. These labels are relative to a given M2; i.e., O3<sub>4</sub> relative to the illustrated M2 is O3<sub>3</sub> relative to the adjacent M2 that is not shown. The labeling of the O atoms around a given M2 can be done by viewing down *a*\* (*a*\* is pointing out of the paper at the reader) and locating the "arrowhead" formed by the two octahedral faces sharing the O1<sub>a</sub>-O1<sub>b</sub> edge northwest of M2. This nomenclature is an alternative to that of Burnham et al. (1967), which gives every atom in the unit cell its own name (in their Fig. 9, O3<sub>1</sub> = O3C2, O3<sub>2</sub> = O3C1, O3<sub>3</sub> = O3D1, and O3<sub>4</sub> = O3D2). This paper uses the nomenclature of Downs (2003) because it provides a single description that applies to every M2 in the structure. O1's have been labeled O1<sub>a</sub> and O1<sub>b</sub> for use in this paper.

oxygen radius,  $r$ . The model equivalent to an observed pyroxene is defined as a model pyroxene with the same  $\theta$  and unit-cell volume as the observed crystal. Thompson et al. (2005) used the TD model to derive an EOS for the data presented in the present paper, and showed that it reproduced observed data as well as the third-order Birch-Murnaghan model. Thompson et al. (2005) also established a relationship between M1 cation radius (Shannon 1976) and unit-cell volume in  $C2/c$  pyroxenes. Bindi et al. (2006) extended this relationship to include compressibility in the case of K-rich clinopyroxene.

The results and discussion section of this paper will compare the observations of previous workers and our new data with the TD model to evaluate the degree to which the model can account for the proposed compressional mechanisms of diopside.

## EXPERIMENTAL METHODS

A clear, colorless single crystal of diopside from DeKalb, New York was kindly provided by the Smithsonian Museum (R18685). This crystal is from the same locality as the sample used in the Levien and Prewitt (1981) study. An untwinned fragment of size  $115 \mu\text{m} \times 110 \mu\text{m} \times 60 \mu\text{m}$  was chosen that exhibited ideal scan profiles with narrow Gaussian full-widths of  $0.08^\circ$  in  $\omega$ .

The crystal was mounted on a Picker diffractometer with unfiltered Mo radiation, automated with a Windows-based Visual-Fortran code extensively modified after the SINGLE software written by Larry Finger and described in Angel et al. (2000).

The peak positions of 50 strong reflections with  $2\theta < 30^\circ$  were determined by the 8-reflection centering technique of King and Finger (1979) and used to refine the unit-cell parameters listed in Table 1. Finger's centering algorithm was modified to include one more cycle of centering over each of three diffractometer angles as well as fitting the final  $\omega$ -scan to the sum of the 2 Gaussian profiles that represent  $K\alpha_1$  and  $K\alpha_2$  scattering. These two modifications improved the error of the fitted cell volume by  $\sim 1$  order of magnitude. The orientation matrix was refined and half a sphere of intensity data were collected to  $2\theta \leq 60^\circ$ , using  $\omega$  scans of  $1^\circ$  width, step size of  $0.025^\circ$  and 5 s per step counting times. The structure was refined on  $F$  with anisotropic displacement factors using a modification of RFINE (Finger and Prince 1975) to an  $R_w = 0.026$ . The refined structure parameters match those reported in Levien and Prewitt (1981) within standard deviation and so are not reported here. Instead, for continuity with the high-pressure data, the structure was refined with isotropic displacement factors to an  $R_w = 0.041$ . Structure factors were weighted by  $w = [\sigma_F^2 + (pF)^2]^{-1}$ , where  $\sigma_F$  was obtained from counting statistics and  $p$  chosen to ensure normally distributed errors (Ibers and Hamilton 1974). An isotropic extinction correction was also applied. The refined structural data are listed in Table 2 and on deposit as cifs<sup>1</sup>.

The diopside crystal was loaded into a 4-pin Merrill Bassett type diamond anvil cell with the diffraction vector  $S(110)$ , defining the cleavage plane, parallel to the cell axis. The diamond anvil culet was  $600 \mu\text{m}$  in diameter. A stainless steel gasket,  $250 \mu\text{m}$  thick, pre-indented to  $100 \mu\text{m}$ , with a hole of  $300 \mu\text{m}$  diameter was used. The gasket began to fail at 5 GPa, so the diamond cell was reloaded with a new gasket and the same crystal in the same orientation for the higher-pressure data collections. A mixture of 15:4:1 methanol:ethanol:water was used as a pressure medium. To determine pressure, a small ruby fragment was included in the cell, and the positions of its R1 and R2 peaks were determined by fitting Lorentzian functions to the fluorescence spectra. The pressure was determined by the equation in Mao et al. (1978) with an estimated error of 0.04 GPa. No peak broadening was observed over the pressure domain of the experiment.

Every accessible reflection allowed by  $C2/c$  symmetry, up to 753 intensity data ( $2\theta \leq 60^\circ$ ), were collected at 9 different pressures to 10.16 GPa, with  $\omega$  scans of  $1^\circ$  width, in steps of  $0.025^\circ$ , and counting times of 10 s per step using the fixed  $\phi$ -mode for data collection (Angel et al. 2000). These data were averaged and reduced to  $\sim 320$  unique reflections. Absorption corrections for the Be seats and diamond anvils were made from a transmission profile of the diamond cell before loading. Intensity data were processed as noted above at room conditions. For each refinement, a distinct value of  $p$  was obtained to adjust the weighting scheme, as mentioned above, to produce a normalized error distribution. This procedure usually produces a poorer  $R_w$ -factor than would have resulted with  $p \equiv 0$ , but the refined structure parameters vary more smoothly over the pressure range of the experiment.

**TABLE 1.** Unit-cell parameters of diopside as a function of pressure (space group  $C2/c$ )

run	$P$ (GPa)	$a$ (Å)	$b$ (Å)	$c$ (Å)	$\beta$ ( $^\circ$ )	$V$ (Å <sup>3</sup> )
0	0.0001*	9.7397(3)	8.9174(3)	5.2503(2)	105.866(3)	438.63(3)
1	0.13(4)*	9.7377(4)	8.9151(3)	5.2494(3)	105.851(4)	438.39(3)
3	2.32(4)*	9.6808(7)	8.8488(5)	5.2180(5)	105.606(6)	430.52(5)
4	3.35(4)	9.6570(4)	8.8201(3)	5.2048(3)	105.497(3)	427.21(3)
5	4.22(4)*	9.6341(4)	8.7948(3)	5.1926(3)	105.421(3)	424.13(3)
7	5.37(4)	9.6079(4)	8.7631(2)	5.1777(2)	105.309(3)	420.46(3)
8	5.11(4)*	9.6135(5)	8.7695(3)	5.1813(2)	105.337(5)	421.25(3)
9	0.0001	9.7405(2)	8.9171(2)	5.2504(2)	105.865(2)	438.66(2)
12	2.98(4)	9.6649(8)	8.8285(5)	5.2088(4)	105.509(7)	428.26(5)
33	7.08(4)*	9.5731(7)	8.7197(6)	5.1580(3)	105.203(6)	415.49(5)
34	8.01(4)*	9.5557(5)	8.6951(4)	5.1474(3)	105.148(5)	412.83(4)
35	8.88(4)*	9.5391(4)	8.6752(4)	5.1385(2)	105.106(4)	410.53(3)
36	9.50(4)*	9.5270(5)	8.6587(4)	5.1306(3)	105.067(5)	408.68(3)
37	10.16(4)*	9.5164(5)	8.6449(4)	5.1246(3)	105.033(5)	407.16(3)

\* Intensity data collected at these pressures.

## RESULTS AND DISCUSSION

A pressure-volume equation of state for diopside was obtained by fitting the weighted data from Table 1 to a third-order Birch-Murnaghan equation (cf. Duffy and Wang 1998), yielding  $V_0 = 438.66(2) \text{ Å}^3$ ,  $K_0 = 118(1) \text{ GPa}$ ,  $K' = 3.8(3)$ . The equation of state obtained by fixing  $K' \equiv 4$  is similar, yielding  $V_0 = 438.66(2) \text{ Å}^3$ ,  $K_0 = 117.1(2) \text{ GPa}$ . The data were fit to the third order Birch-Murnaghan equation using the Levenberg-Marquardt algorithm (Press et al. 1992). A statistical analysis of the fitted data provides the estimate of 0.04 GPa as the error in pressure. The data and the fitted curve are presented in Figure 2. The fitted values for  $K_0$  agree particularly well with the Voigt averages of 117(1) and 118(4) reported by Levien et al. (1979) and Aleksandrov et al. (1961), respectively.

The parameters for an equation of state are particularly sensitive to the fitting algorithm that is used, primarily because it is a nonlinear problem. Therefore, we compare our equation of state with those from previous studies by fitting their data using our algorithm (Fig. 2). A comparison of the results yields the parameters shown in Table 3.

The data from Levien and Prewitt (1981) fall on our fitted  $P$ - $V$  curve and can be considered statistically identical. The Tribaudino et al. (2000) data are from a powder diffraction study to 40.8 GPa with nitrogen as a pressure medium. They observed gas-solid as well as several solid-solid phase transitions in the pressure medium, and they also suggest that the diopside underwent the  $C2/c$ - $C2/c$  phase change that Chopelas and Serghiou (2002) observed with Raman spectroscopy. For these reasons it is likely that the parameters fitted to their data are not representative of the same set of conditions as in the present study. By inspection, however, the Tribaudino et al. (2000) data to 10 GPa fall on our fitted curve. The data from Zhang et al. (1997) fall significantly off the trend of the other three datasets. Their study used a synthetic single crystal in much the same set of experimental conditions as in the present study.

The refined structural parameters were used to compute relevant interatomic distances, angles and polyhedral volumes

<sup>1</sup> Deposit item AM-08-006, cif. Cif deposit items are available via the MSA web site at <http://www.minsocam.org>, go to the American Mineralogist Contents, find the table of contents for the specific volume/issue wanted, and then click on the deposit link there.

**TABLE 2.** Refined structural parameters for diopside and model equivalents as a function of pressure

<i>P</i> (GPa)	1 atm	model	0.13	model	2.32	model	4.22	model	5.11	model
<i>R<sub>w</sub></i>	0.041		0.060		0.055		0.051		0.039	
<i>p</i>	0.035		0.053		0.050		0.045		0.035	
Mg1 <i>y</i>	0.908083(97)	11/12	0.90811(19)	11/12	0.90867(18)	11/12	0.90951(17)	11/12	0.90961(13)	11/12
<i>B<sub>iso</sub></i>	0.31(2)		0.46(4)		0.37(4)		0.49(4)		0.38(3)	
Ca2 <i>y</i>	0.301478(61)	1/4	0.30167(12)	1/4	0.30270(11)	1/4	0.30368(11)	1/4	0.304111(86)	1/4
<i>B<sub>iso</sub></i>	0.65(2)		0.82(4)		0.72(3)		0.85(3)		0.67(2)	
Si <i>x</i>	0.286187(55)	0.308229	0.28615(14)	0.30824	0.28626(14)	0.30828	0.28618(13)	0.30830	0.28607(13)	0.30832
<i>y</i>	0.093189(55)	1/12	0.09324(11)	1/12	0.09370(10)	1/12	0.09426(10)	1/12	0.094506(81)	1/12
<i>z</i>	0.229355(99)	0.267735	0.22913(19)	0.26733	0.22834(19)	0.26540	0.22772(18)	0.26438	0.22734(14)	0.26368
<i>B<sub>iso</sub></i>	0.34(2)		0.51(4)		0.43(3)		0.59(3)		0.47(2)	
O1 <i>x</i>	0.11554(15)	0.133541	0.11566(40)	0.13352	0.11547(37)	0.13344	0.11512(34)	0.13339	0.11566(33)	0.13336
<i>y</i>	0.08690(15)	1/12	0.08721(30)	1/12	0.08705(29)	1/12	0.08768(28)	1/12	0.08821(21)	1/12
<i>z</i>	0.14186(27)	0.163226	0.14245(53)	0.16304	0.14258(49)	0.16214	0.14162(48)	0.16166	0.14191(38)	0.16134
<i>B<sub>iso</sub></i>	0.55(3)		0.75(6)		0.62(5)		0.77(5)		0.64(4)	
O2 <i>x</i>	0.36094(15)	0.366459	0.36112(42)	0.36648	0.36079(41)	0.36656	0.36057(37)	0.36661	0.35967(33)	0.36664
<i>y</i>	0.25019(15)	1/4	0.25050(31)	1/4	0.25183(31)	1/4	0.25337(30)	1/4	0.25385(22)	1/4
<i>z</i>	0.31776(27)	0.336774	0.31808(53)	0.33696	0.31872(53)	0.33786	0.31985(47)	0.33834	0.31975(38)	0.33866
<i>B<sub>iso</sub></i>	0.62(2)		0.80(5)		0.71(5)		0.90(5)		0.67(4)	
O3 <i>x</i>	0.35073(14)	0.366459	0.35099(39)	0.36648	0.35156(37)	0.36656	0.35221(32)	0.36661	0.35316(33)	0.36664
<i>y</i>	0.01744(15)	0.017102	0.01778(30)	0.01743	0.01943(28)	0.01902	0.02031(27)	0.01986	0.02091(20)	0.02043
<i>z</i>	0.99543(26)	0.035469	0.99527(52)	0.03466	0.99227(49)	0.03079	0.99045(46)	0.02875	0.99051(38)	0.02736
<i>B<sub>iso</sub></i>	0.56(3)		0.69(5)		0.60(5)		0.77(5)		0.66(4)	
<i>P</i> (GPa)	7.08	model	8.01	model	8.88	model	9.50	model	10.16	model
<i>R<sub>w</sub></i>	0.042		0.043		0.037		0.037		0.045	
<i>p</i>	0.032		0.034		0.027		0.028		0.030	
Mg1 <i>y</i>	0.90984(19)	11/12	0.90998(20)	11/12	0.91042(20)	11/12	0.91060(21)	11/12	0.91075(24)	11/12
<i>B<sub>iso</sub></i>	0.40(4)		0.41(4)		0.41(3)		0.39(3)		0.44(4)	
Ca2 <i>y</i>	0.30480(12)	1/4	0.30528(13)	1/4	0.30559(13)	1/4	0.30588(13)	1/4	0.30587(16)	1/4
<i>B<sub>iso</sub></i>	0.71(3)		0.73(3)		0.69(3)		0.70(3)		0.67(3)	
Si <i>x</i>	0.28616(15)	0.30835	0.28595(15)	0.30836	0.28632(14)	0.30836	0.28614(15)	0.30839	0.28610(17)	0.30840
<i>y</i>	0.09503(11)	1/12	0.09523(12)	1/12	0.09520(11)	1/12	0.09547(12)	1/12	0.09554(14)	1/12
<i>z</i>	0.22743(19)	0.26246	0.22701(20)	0.26231	0.22734(19)	0.26199	0.22733(20)	0.26085	0.22718(23)	0.26082
<i>B<sub>iso</sub></i>	0.48(3)		0.51(3)		0.50(3)		0.50(3)		0.47(3)	
O1 <i>x</i>	0.11519(39)	0.13330	0.11494(40)	0.13329	0.11525(35)	0.13327	0.11520(37)	0.13321	0.11538(43)	0.13321
<i>y</i>	0.08817(29)	1/12	0.08890(31)	1/12	0.08839(29)	1/12	0.08809(30)	1/12	0.08832(35)	1/12
<i>z</i>	0.14212(50)	0.16077	0.14173(52)	0.16070	0.14192(49)	0.16055	0.14222(52)	0.16001	0.14178(59)	0.16000
<i>B<sub>iso</sub></i>	0.62(5)		0.69(5)		0.58(5)		0.65(5)		0.57(6)	
O2 <i>x</i>	0.35924(40)	0.36670	0.35903(41)	0.36671	0.35930(37)	0.36673	0.35914(39)	0.36679	0.35921(45)	0.36679
<i>y</i>	0.25493(33)	1/4	0.25554(35)	1/4	0.25638(33)	1/4	0.25645(34)	1/4	0.25714(40)	1/4
<i>z</i>	0.32145(50)	0.33923	0.32144(52)	0.33930	0.32204(49)	0.33945	0.32137(51)	0.33999	0.32226(59)	0.34000
<i>B<sub>iso</sub></i>	0.72(5)		0.77(5)		0.71(5)		0.68(5)		0.68(6)	
O3 <i>x</i>	0.35263(39)	0.36670	0.35425(39)	0.36671	0.35290(37)	0.36673	0.35342(39)	0.36679	0.35409(46)	0.36679
<i>y</i>	0.02196(30)	0.02143	0.02211(31)	0.02156	0.02239(30)	0.02182	0.02336(31)	0.02276	0.02340(36)	0.02279
<i>z</i>	0.98889(52)	0.02493	0.98887(52)	0.02461	0.98742(50)	0.02398	0.98756(52)	0.02170	0.98725(61)	0.02163
<i>B<sub>iso</sub></i>	0.69(5)		0.65(5)		0.67(5)		0.65(5)		0.67(6)	

Notes: Mg1 and Ca2 are located at special positions [0 *y* ¼]. Model equivalents have regular M1, T, and the same O3-O3-O3 angle,  $\theta$ , and unit-cell volume as the observed pyroxenes.

(Table 4). The polyhedral volumes were fit with the same Birch-Murnaghan expression that was used to compute the bulk modulus for the unit-cell volume, and resulted in  $K_0$  values of 102(4), 105(4), and 300(21) GPa for CaO<sub>8</sub>, MgO<sub>6</sub>, and SiO<sub>4</sub>, respectively, with  $K' \equiv 4$ . Thompson et al. (2005) described a relationship between ambient unit-cell volume and M1 cation radius in C2/*c* pyroxenes, and speculated that M1 might also be controlling compressibility. If the relationship between volume and M1 holds at pressure, one would expect to see a relationship between  $K_0$  for the unit cell and  $K_0$  for M1 across the C2/*c* pyroxenes. An attempt was made to assess this idea by looking

**TABLE 3.** Comparison of recalculated EOS parameters from previous works on diopside with this work

<i>V<sub>0</sub></i> (Å <sup>3</sup> )	<i>K<sub>0</sub></i> (GPa)	<i>K'</i>	Reference
439.13(6)	113(3)	5(1)	Levien and Prewitt (1981) to 5.3 GPa
438.4(1)	110(2)	4.9(5)	Zhang et al. (1997) to 9.97 GPa
439.47(2)	104(1)	7.1(2)	Tribaudino et al. (2000) to 40.8 GPa
438.66(2)	118(1)	3.8(2)	This study to 10.16 GPa

at the pressure data sets for diopside, jadeite (McCarthy et al. 2008), kosmochlor (Origlieri et al. 2003), hedenbergite (Zhang et al. 1997), and K-cpx (Bindi et al. 2006). Unconstrained fits to M1 resulted in very large standard deviations. Constraining



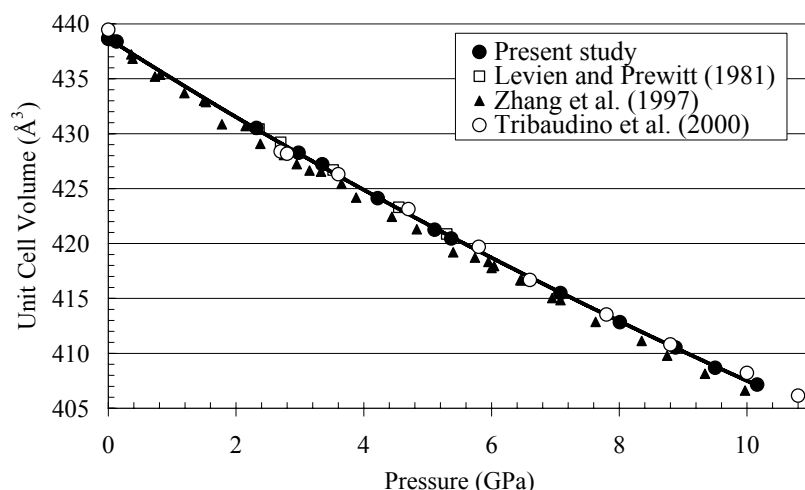


**FIGURE 2.** A plot of the unit-cell volume of diopside as a function of pressure. The solid line represents the Birch-Murnaghan curve fitted to the data from the present study in Table 1. Data from three other studies of diopside are also plotted for comparison.

**TABLE 4.** Selected geometrical parameters for diopside as a function of pressure

P (GPa)	1 atm	0.13	2.32	4.22	5.11	7.08	8.01	8.88	9.50	10.16
R(Si-O1) (Å)	1.600(1)	1.598(4)	1.594(4)	1.590(4)	1.581(3)	1.581(4)	1.578(4)	1.577(4)	1.574(4)	1.570(4)
R(Si-O2) (Å)	1.588(1)	1.591(3)	1.587(3)	1.587(3)	1.582(2)	1.578(3)	1.578(3)	1.581(3)	1.576(3)	1.580(4)
R(Si-O3 <sub>1</sub> ) (Å)	1.668(1)	1.668(3)	1.664(3)	1.662(2)	1.660(2)	1.654(3)	1.659(3)	1.652(3)	1.650(3)	1.653(4)
R(Si-O3 <sub>2</sub> ) (Å)	1.685(1)	1.688(3)	1.682(3)	1.679(3)	1.684(2)	1.678(3)	1.680(3)	1.670(3)	1.675(3)	1.675(3)
<R(Si-O)> (Å)	1.635	1.636	1.632	1.630	1.627	1.623	1.624	1.620	1.619	1.620
V(SiO <sub>4</sub> ) (Å <sup>3</sup> )	2.224	2.228	2.210	2.201	2.190	2.174	2.177	2.164	2.160	2.161
R(Ca-O1) (Å)	2.366(1)	2.364(3)	2.354(3)	2.343(2)	2.338(2)	2.327(3)	2.319(3)	2.321(3)	2.320(3)	2.316(4)
R(Ca-O2) (Å)	2.349(1)	2.348(3)	2.341(3)	2.334(2)	2.336(2)	2.326(3)	2.325(3)	2.321(3)	2.323(3)	2.318(3)
R(Ca-O3 <sub>23</sub> ) (Å)	2.559(1)	2.558(3)	2.552(3)	2.540(2)	2.532(2)	2.528(3)	2.514(3)	2.518(3)	2.516(3)	2.511(4)
R(Ca-O3 <sub>14</sub> ) (Å)	2.721(1)	2.716(3)	2.668(3)	2.632(2)	2.614(2)	2.589(3)	2.569(3)	2.564(3)	2.551(3)	2.542(4)
<R(Ca-O)> (Å)	2.499	2.497	2.479	2.462	2.455	2.443	2.432	2.431	2.427	2.422
V(CaO <sub>6</sub> ) (Å <sup>3</sup> )	25.779	25.719	25.222	24.760	24.572	24.251	23.938	23.931	23.841	23.679
R(Mg-O1 <sub>2</sub> ) (Å)	2.117(1)	2.118(3)	2.096(3)	2.082(3)	2.081(2)	2.065(3)	2.063(3)	2.054(3)	2.046(3)	2.046(4)
R(Mg-O1 <sub>3</sub> ) (Å)	2.058(1)	2.061(3)	2.053(3)	2.041(3)	2.041(2)	2.034(3)	2.029(3)	2.027(3)	2.026(3)	2.023(3)
R(Mg-O2) (Å)	2.051(1)	2.048(4)	2.032(3)	2.020(3)	2.018(3)	2.009(3)	2.003(4)	1.996(3)	1.993(3)	1.988(4)
<R(Mg-O)> (Å)	2.075	2.076	2.061	2.048	2.047	2.036	2.032	2.026	2.022	2.019
V(MgO <sub>6</sub> ) (Å <sup>3</sup> )	11.824	11.829	11.576	11.363	11.352	11.171	11.093	11.002	10.940	10.894
Si-O3-Si (°)	135.83(7)	135.6(2)	135.0(2)	134.4(2)	133.8(2)	133.9(2)	132.9(2)	133.7(2)	133.2(2)	132.7(3)
O3-O3-O3 (°)	166.53(9)	166.2(2)	165.0(2)	164.4(2)	163.9(2)	163.1(2)	163.0(2)	162.8(2)	162.1(2)	162.0(2)

Note: Nomenclature after Downs (2003). See Figure 1.

$K' \equiv 4$  resulted in smaller errors, but in some cases changed  $K_0$  considerably because unconstrained  $K'$  ranged as low as 2, and did not produce the expected trend. Because it was not possible to get meaningful values for the compressibilities and first derivatives of the M1 octahedra, the well-determined quantity  $\langle R(M1-O) \rangle$  was elected parameter of choice in the search for any volume-M1 site systematics with pressure. At ambient conditions, a plot of unit-cell volume vs. M1 cation size displays a highly correlated linear trend (Thompson et al. 2005). Using  $\langle R(M1-O) \rangle$  instead of cation size, since there is no conventional definition for cation sizes at pressure, it seemed reasonable that the unit-cell volume decrease at pressure might follow along the ambient unit-cell volume vs.  $\langle R(M1-O) \rangle$  curve that results from varying M1 chemistry. However, these pyroxenes show a greater decrease in volume when M1 "cation size" undergoes pressure-induced shrinkage than they do when M1 cation size shrinks by altering chemistry. Nonetheless, Bindi et al. (2006) obtained results suggesting that M1 composition plays an important role in controlling compression.

Unit-strain ellipsoids (Table 5) were computed with the

cell-parameter data between room and pressure conditions using Ohashi's STRAIN software (Hazen and Finger 1982) and our own code based on the algorithm reported in Hazen et al. (2000). The unit strain ellipsoid is significantly anisotropic, as demonstrated by the axial ratios  $\epsilon_1:\epsilon_2:\epsilon_3 = 1.2:1.7:2.05$  (computed between 0–10.16 GPa), where  $\epsilon_2$  is parallel to the **b** axis. As a function of pressure, there is no change in the magnitude of the unit strain parallel to the stiffest direction,  $\epsilon_1$ , and very little change in its orientation, which approximately bisects the angle between the **a** and **c** axes. The other two ellipsoid axes are roughly equal in length and stiffen with increasing pressure as illustrated in Figure 3a.

The anisotropy of unit-cell compression in pyroxenes has been discussed by Zhang et al. (1997), Tribaudino et al. (2000), and analyzed in depth by Origlieri et al. (2003), who showed that the orientations of the ellipsoidal axes are related to directions of closest packing in pyroxenes. Thompson and Downs (2004) showed that the TD model, based on kinking of chains of rigid tetrahedra combined with isotropic compression, produced anisotropic strain ellipsoids with similar orientations to those

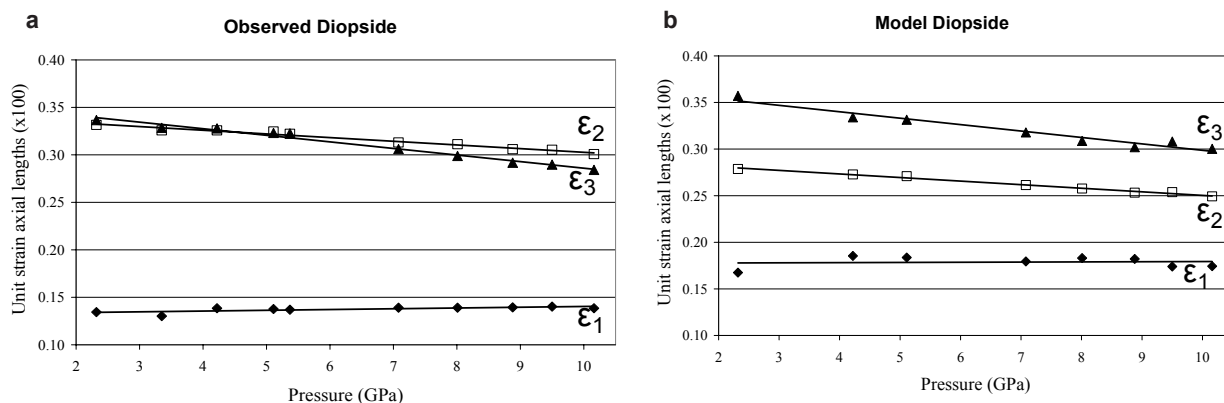


**FIGURE 3.** (a) A plot of the unit strain axial lengths of diopside as a function of pressure. Each point represents the strain between the unit-cell volumes at the plotted pressures vs. that at room pressure. The solid lines represent linear least-squares fits to the data only to guide the eye. (b) A plot of the unit strain axial lengths of the model equivalents to diopside as a function of pressure.

**TABLE 5.** Unit strain ellipsoids as a function of pressure computed with Ohashi's STRAIN software

P (GPa)	2.32	3.35	4.22	5.11	5.37	7.08	8.01	8.88	9.50	10.16
$-\epsilon_1$	0.134(4)	0.130(2)	0.139(2)	0.138(1)	0.137(1)	0.139(1)	0.139(1)	0.1394(8)	0.1402(8)	0.1385(8)
$-\epsilon_2 // \mathbf{b}$	0.332(3)	0.326(1)	0.326(2)	0.325(3)	0.322(6)	0.313(1)	0.3112(6)	0.3059(7)	0.3054(6)	0.3008(6)
$-\epsilon_3$	0.337(3)	0.328(1)	0.328(2)	0.323(4)	0.323(6)	0.306(1)	0.2988(7)	0.2917(6)	0.2898(6)	0.2841(5)
$\angle \epsilon_1 \wedge \mathbf{a}$ (°)	52.3(8)	52.2(4)	52.5(3)	52.5(2)	52.2(2)	51.9(3)	51.5(2)	51.6(2)	51.1(2)	51.1(2)
$\angle \epsilon_1 \wedge \mathbf{c}$ (°)	53.5(8)	53.6(4)	53.4(3)	53.4(2)	53.7(2)	54.0(3)	54.4(2)	54.3(2)	54.8(2)	54.8(2)
$\angle \epsilon_3 \wedge \mathbf{a}$ (°)	142.3(8)	142.2(4)	142.5(5)	142.5(8)	142(1)	141.9(3)	141.5(2)	141.6(2)	141.1(2)	141.1(2)
$\angle \epsilon_3 \wedge \mathbf{c}$ (°)	36.5(8)	36.4(4)	36.6(5)	36.6(8)	36(1)	36.0(3)	35.6(2)	35.7(2)	35.3(2)	35.2(2)

Notes: The strain was computed between room conditions and  $P$ . The axis labeled  $\epsilon_2$  is parallel to the  $\mathbf{b}$  axis,  $\epsilon_1$  and  $\epsilon_3$  lie in the  $\mathbf{ac}$ -plane perpendicular to each other, and  $\epsilon_1$  divides  $\beta$ . The magnitudes of  $\epsilon$  have been multiplied by 100.

**TABLE 6.** A comparison of the polyhedral distortion parameters bond angle variance ( $\sigma$ ) and quadratic elongation ( $\lambda$ ) (Robinson et al. 1971) for diopside at pressures to 10 GPa and forsterite at ambient conditions, showing that M1 and T in diopside are nearly regular

	P (GPa)	$\sigma_T$	$\lambda_T$	$\sigma_{M1}$	$\lambda_{M1}$	$\sigma_{M2}$	$\lambda_{M2}$
forsterite	0.0001	49.53	1.011	96.34	1.027	90.67	1.026
diopside	0.0001	27.87	1.007	17.79	1.005	358.5	1.372
diopside	0.13	27.96	1.007	17.60	1.005	358.1	1.374
diopside	2.32	27.78	1.007	17.22	1.005	363.0	1.382
diopside	4.22	28.27	1.007	17.24	1.005	365.8	1.382
diopside	5.11	28.36	1.007	16.97	1.005	365.1	1.379
diopside	7.08	27.26	1.007	17.40	1.005	367.1	1.382
diopside	8.01	29.45	1.007	18.11	1.005	369.6	1.380
diopside	8.88	26.62	1.006	17.21	1.005	367.7	1.382
diopside	9.50	27.65	1.006	17.08	1.005	369.7	1.383
diopside	10.16	28.64	1.006	16.99	1.005	369.6	1.380

Note: The distortion parameters for M2 in diopside are calculated for the octahedron formed by Ca and its six nearest-neighbor O atoms.

observed experimentally.

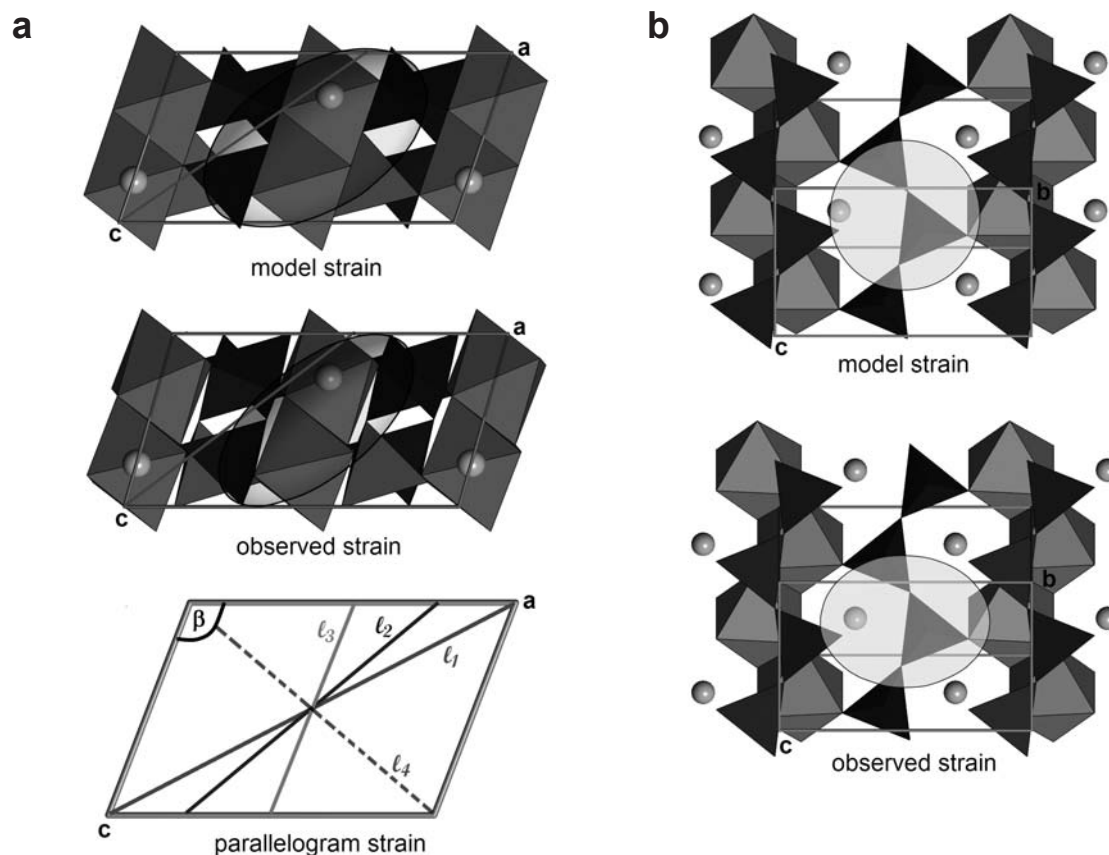
Model equivalents to each of the diopside structures determined at various pressures were calculated using the algorithm of Thompson and Downs (2004). Each model diopside has regular M1 and T and the same unit-cell volume and O3-O3-O3 angle,  $\theta$ , as its corresponding observed structure.

Table 6 provides quantitative evidence that diopside topology is close to that of the TD model. Traditional measures of polyhedral distortion computed for diopside at pressure show that T and M1 are approximately regular. Table 6 compares the angle variance and quadratic elongation (Robinson et al. 1971) for the T, M1, and M2 polyhedra in diopside with forsterite. Olivines have long been described as having nearly closest-packed oxygen arrangements (cf. Megaw 1973) and Thompson

and Downs (2001) demonstrated this quantitatively. Thus, olivine polyhedra should be relatively undistorted. Despite the fact that the bulk structural distortion of the pyroxene structure is greater than that of olivine, often by a factor of three or more (Thompson and Downs 2001), the M1 and T polyhedra in pyroxene are significantly less distorted than the octahedra and tetrahedra in forsterite.

Unit strain ellipsoids calculated for the model have similar orientation and anisotropy to those observed, with  $\epsilon_1:\epsilon_2:\epsilon_3 = 1:1.43:1.72$  (vs.  $1:2.17:2.05$ ) and  $\angle \epsilon_1 \wedge \mathbf{a} = 58.23^\circ$  (vs.  $51.10^\circ$ ). Comparing Figures 3a and 3b shows that the changes in the axial lengths of the strain ellipsoid with pressure in the model trend parallel to their observed diopside counterparts, but have different initial ( $P=0$  GPa) values. In particular, observed diopside is much more compressible along  $\mathbf{b}$  than its model equivalent, so that observed  $\epsilon_2$  at  $P=0$  GPa is much larger than model  $\epsilon_2$ . Thus, the plot of model  $\epsilon_2$  vs. pressure is parallel to observed  $\epsilon_2$  vs. pressure, but the observed curve is well above the model curve. Therefore, kinking of the tetrahedral chains alone is sufficient to explain the changes in compressibility along the principle axes of the strain ellipsoid with pressure, but not the absolute magnitudes of these compressibilities, particularly along  $\mathbf{b}$ . This means that changes in compressibility in diopside between 0 and 10 GPa do not require a change in compression mechanism, and that the compression in diopside along  $\mathbf{b}$  occurs via at least one other mechanism in addition to tetrahedral chain kinking and isotropic scaling of the structure.

The strain ellipsoids for diopside and its model equivalent between room conditions and 10.16 GPa are illustrated in Figure 4, overlaying cartoons of the crystal structures. Most of the



**FIGURE 4.** (a) Strain ellipsoids in the *a-c* plane overlying cartoons of the model and observed structures. The solid red line represents the direction of maximum strain in the *a-c* plane due to the change in  $\beta$ . The parallelogram illustrates this geometric principle without the scaling inherent to strain calculations. (b) Cross-sections of the strain ellipsoid parallel to the *b-c* plane overlying cartoons of the crystal structure.

anisotropy in the *a-c* plane in these ellipsoids is a consequence of the change in  $\beta$  with pressure. This geometric principle is illustrated in Figure 4a. Decreasing  $\beta$  in a parallelogram with fixed edge lengths results in an overall volume increase with a maximum compression along line  $\ell_1$ :  $d(\ell_1)/d\beta = -2a\sin\beta = 2[d(\ell_3)/d\beta] = -[d(\ell_4)/d\beta]$ . Line  $\ell_3$  is constant. Unit strain ellipsoids are normalized so that  $a/c = 1$ , but the parallelogram in Figure 4a is not normalized. Therefore, the direction of normalized maximum compression in the model and observed structures due to changes in  $\beta$  is not along  $[1\ 0\ 1]$ , but along  $[c/a\ 0\ 1]$ . This direction is illustrated in Figure 4a as a solid line parallel to  $[c/a\ 0\ 1]$ . The change in model  $\beta$  results from tetrahedral rotation, and accounts for ~85% of the observed change in  $\beta$ . Kinking of the tetrahedral chains is sufficient to explain most of the compressional anisotropy in the *a-c* plane. Since the observed change in  $\beta$  is 15% greater than the model change, the observed *a-c* plane anisotropy is also greater. Arbitrarily forcing the magnitude of change in model  $\beta$  to match the observed value alters model  $\epsilon_1:\epsilon_3$  from 1:1.72 to 1:1.93, much closer to the observed value of 1:2.05. An explanation for the larger observed change in  $\beta$  is proposed later in the manuscript. Tetrahedral rotation accounts for most of the shearing noted by Downs et al. (1999), Tribaudino et al. (2000), and Downs (2003).

Change in the *c/a* ratio also affects the orientation and

anisotropy of the ellipsoid. The observed *c/a* ratio decreases slightly between 0 and 10.16 GPa in diopside, so the direction of maximum compression in the *a-c* plane,  $\epsilon_3$ , is rotated slightly counterclockwise relative to the line (Fig. 4a) that indicates the direction of maximum compression due to change in  $\beta$ . In the model, *c/a* increases slightly with compression, so  $\epsilon_3$  is rotated slightly clockwise instead. Additionally, the slight decrease in observed *c/a* exaggerates the anisotropy due to the change in  $\beta$ , while the slight increase in model *c/a* compensates for some of the anisotropy due to the change in  $\beta$ .

Cross-sections through the model and observed strain ellipsoids parallel to the *b-c* plane are illustrated in Figure 4b (*b*-axis parallel  $\epsilon_2$ ). The model cross-section is a circle because *b/c* is constant at  $\sqrt{3}$ . The *b* direction is the most compressible direction in observed diopside. Ambient *b/c* is less than model (1.70 vs. 1.73) and decreases to 1.69 at 10.16 GPa. The relatively greater compression parallel to *b* is accommodated by a relative narrowing of the M1 chain (i.e., O2 atoms form the outer edges of the M1 chain and move with relatively large displacements toward the chain axis with pressure, Fig. 5). Strain across the M1 chain in the *b* direction is  $-0.0575$ , while strain between the chains is  $-0.0036$ . This gives an overall strain parallel to *b* of  $-0.0306$ , compared to  $-0.0239$  along *c*. The component of the O1-O1 separation (M1-M1 shared edge) parallel to *b* is only 25%

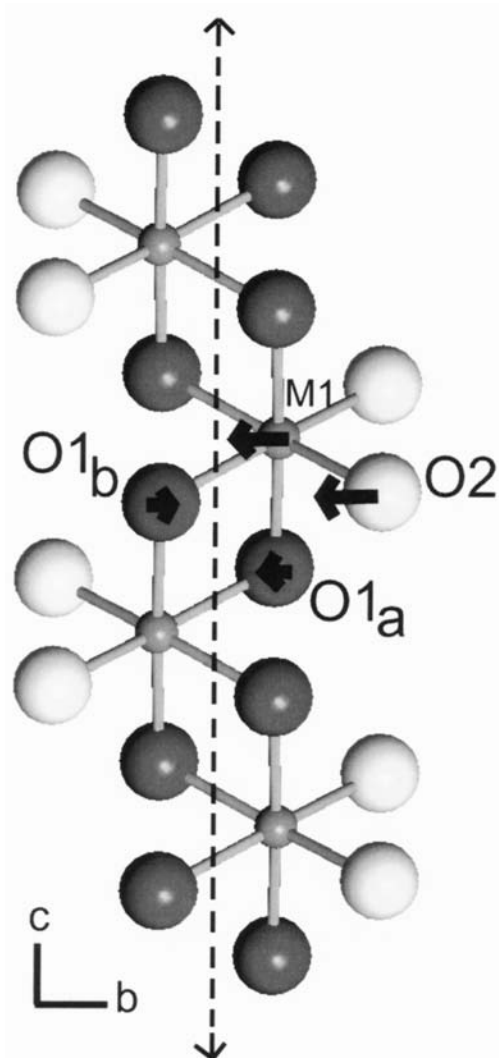


**FIGURE 5.** A ball-and-stick cartoon of the M1 chain in diopside at room conditions. The “axis” of the chain parallel to *c* is illustrated as a dotted line. Under compression, the M1 chain collapses parallel to *b* toward its axis with more strain than in any other part of the structure in any direction. The O1<sub>a</sub>-O1<sub>b</sub> shared edge stays relatively stable parallel to *b*, while O2 and M1 collapse quickly. Compressional anisotropies between the various bonds result from the chain geometry. M1 and O1<sub>b</sub> are moving toward each other, while M1 and O1<sub>a</sub> are moving in parallel. Thus M1-O1<sub>b</sub> shortens more.

as compressible as the chain in that direction, but the M1-M1 component is slightly more compressible than the chain. In the *c* direction, the O1-O1 shared edge is slightly more compressible than the unshared O1-O1 edge. To summarize the behavior of the M1 chain in the *b*-*c* plane, the strain across the shared edge is relatively small in the *b* direction and is approximately equal to the strain of *c* itself in the *c* direction, but the strain in the *b*-direction between the outer edges of the chain is much greater than either of these (Fig. 5), large enough to make [010] the most compressible direction in diopside. The relative incompressibility between the M1 chains affects the tilting of the tetrahedra by al-

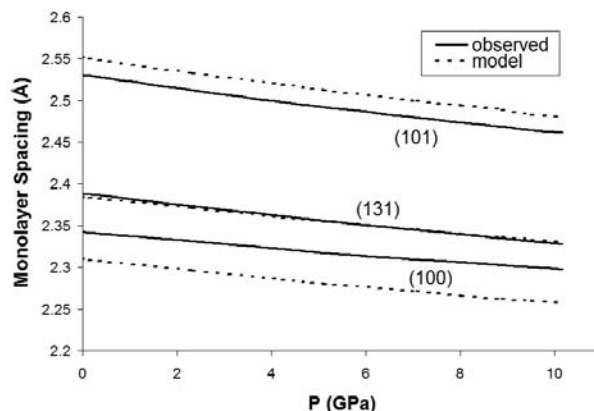


**FIGURE 6.** Spacings between close-packed monolayers in diopside and its model equivalent as a function of pressure. Spacings for the fourth stacking direction, (1 $\bar{3}$ 1), are constrained by geometry to equal those for (131).

lowing the basal faces of the tetrahedra to become more parallel to the *b*-*c* plane with increasing pressure.

Levien and Prewitt (1981) hypothesized that the directions and compressibilities of the M1 and M2 bonds control compression in diopside. In particular, they noted that the very compressible M2-O3<sub>1,4</sub> bonds are oriented 45° between the two principal axes of the strain ellipsoid that compress the most. The data in Table 7 show that model compression by isotropic scaling combined with tetrahedral rotation reproduces most of the M2-O3<sub>1,4</sub> bond compression and the anisotropy between the M2-O3<sub>1,4</sub> bonds and the M2-O3<sub>2,3</sub> bonds. Thus, M2-O3 compressional systematics are not a controlling mechanism, but the consequence of the model mechanisms of tetrahedral chain kinking and isotropic scaling.

M1-O bond compression systematics result from the collapse parallel to *b* of the M1 chain toward its axis (the dotted line in Fig. 5) as described in the preceding paragraph. The positions of O1<sub>a</sub> and O1<sub>b</sub> are relatively stable in comparison to the positions of M1 and O2. In other words, M1 and O<sub>2</sub> move a greater distance parallel to *b* toward the chain axis with pressure than does O1. Since, the components of motion parallel to *b* of M1 and O1<sub>a</sub> are toward each other, while M1 and O1<sub>b</sub> are moving in parallel (Fig. 5), M1-O1<sub>a</sub> compresses more. The motion toward the axis by O<sub>2</sub> gives M1-O2 a compression close to that of M1-O1<sub>a</sub>. The M2-O1 and M2-O2 systematics are analogous to the M1-O1<sub>a</sub> and M1-O1<sub>b</sub> systematics, respectively.

Zhang et al. (1997) observed that the compressibility of the polyhedral units (7.3%) in hedenbergite is greater than that of the voids (6.7%) and concluded that the unit-cell volume compression is dependent upon the polyhedral compressibilities. The analogous compressibilities for diopside between 0.0001 and 10.16 GPa are 7.5% for polyhedra and 7.0% for voids. The model closely reproduces these results with values of 7.6 and 6.9% for polyhedra and voids, respectively. Thus, what Zhang et al. (1997) observed was a consequence of the change in tetrahedral chain geometry combined with isotropic scaling of the structure.

Origlieri et al. (2003) correlated the axes of the strain ellipsoids in several pyroxenes with the stacking directions of close-packed oxygen monolayers and suggested that differences in



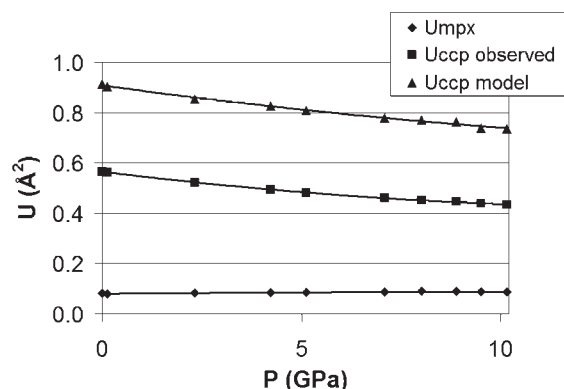


**FIGURE 7.** Distortion parameters for diopside as a function of pressure.  $U_{MPX}$  is a measure of the distortion of observed diopside from its model equivalent, and  $U_{CCP}$  is a measure of the distortion of the anion skeleton of a structure from ideal cubic closest-packed. For each parameter, a value of zero signifies a perfect match and larger positive values represent larger degrees of distortion. A value of one represents a very large degree of distortion.

**TABLE 7.** Comparison of bond length shortening in diopside and its model equivalent between 0 and 10.16 GPa

Bond	% shortening observed	% shortening model
Ca-O1	2.1	2.5
Ca-O2	1.3	2.5
Ca-O3 <sub>2,3</sub>	1.9	0.1
Ca-O3 <sub>1,4</sub>	6.6	5.3
Mg-O1 <sub>a</sub>	3.4	2.5
Mg-O1 <sub>b</sub>	1.7	2.5
Mg-O2	3.1	2.5

inter-monolayer spacings were controlling compression. Figure 6 shows that the observed differences in inter-monolayer spacings are reproduced by the TD model. Therefore, changes in inter-monolayer spacings in diopside are a result of tetrahedral chain kinking and isotropic scaling of the structure, not a mechanism controlling compression.

To summarize, there are three main mechanisms controlling the compression of diopside: isotropic scaling of the structure, tetrahedral chain kinking, and collapse of the M1 chain in the **b**-direction toward its axis, which runs parallel to **c**. Tetrahedral chain kinking decreases  $\beta$ , which creates compressional anisotropy in the **a-c** plane, and the collapse of the M1 chain toward its axis makes **b** the most compressible direction, and creates compressional anisotropy in the **b-c** plane.

Figure 7 compares the distortion of observed diopside from its model equivalent ( $U_{MPX}$ ), the distortion of observed diopside's anion skeleton from cubic closest-packing ( $U_{CCP}$  observed), and the distortion of the model pyroxene's anion skeleton from cubic closest-packing ( $U_{CCP}$  model).  $U_{CCP}$  is described in Thompson and Downs (2001).  $U_{MPX}$  is directly comparable to  $U_{CCP}$  and is calculated by rotating and translating the observed and model pyroxenes relative to each other until the average distance<sup>2</sup> between observed and corresponding model atoms for a  $2 \times 2 \times 4$  block of unit cells (640 atoms) is minimized. Larger values of  $U$  signify greater distortion: 0 is a perfect match, 1 is quite

distorted.

Figure 7 shows that observed diopside is very nearly model, yet the anion skeleton of the observed pyroxene is much less distorted from CCP than the model. This is because the anions in observed diopside are displaced en masse from their model positions toward eutaxy. Figure 7 shows that anion-anion interactions are important in determining diopside's distortion from model. While the model is more distorted from closest-packed than observed diopside, the changes in model and observed diopside's  $U_{CCP}$  with pressure parallel each other, suggesting that model behavior accounts for observed diopside's decrease in distortion from closest-packed with pressure.

Anion-anion interactions are reflected in ambient  $\beta$ 's (model =  $108.7^\circ$ , observed =  $105.9^\circ$ , ideal CCP =  $100.0^\circ$ ) and the compressional behavior of  $\beta$  (decreases more than model). Thus, the observed  $\beta$  is significantly closer to the CCP ideal value than the model equivalent  $\beta$ , and the observed  $\beta$  moves toward the ideal value faster than the model  $\beta$  with pressure. Anion-anion interactions are distorting diopside from perfectly model by small movements of the oxygen atoms away from their model positions toward cubic closest-packing. The influence of anion-anion interactions is also evident in Figure 6, the comparison of observed and model oxygen inter-monolayer spacings. In an ideal CCP pyroxene, all inter-monolayer spacings are equal. The spacings in observed diopside are more uniform than in its model equivalent, which is closer to the ideal CCP arrangement, a result that we attribute to the effect of anion-anion repulsion.

Thompson and Downs (2004) suggested that tetrahedral chain geometry (O3-O3-O3 angles) in  $C2/c$  pyroxenes results from a compromise between opposing M2-T and T-T cation repulsions. Bonded interactions in diopside form a rigid chain of  $MgO_6$  octahedra and a flexible chain of  $SiO_4$  tetrahedra. Ca-Si and Si-Si repulsions distort the structure away from its ideal CCP configuration through rigid-body rotation of the tetrahedra, determining tetrahedral chain geometry. Anion-anion interactions drive small adjustments toward eutaxy to the extent that the dominating bonded interactions and cation-cation repulsions allow.

## ACKNOWLEDGMENTS

We thank the National Science Foundation for funding our study, Compression Mechanisms of Upper Mantle Minerals, through grant no. EAR-9903104. We also thank our Associate Editor, G.D. Gatta, reviewer F. Nestola, and an anonymous referee for their valuable suggestions.

## REFERENCES CITED

- Aleksandrov, K.S. and Rythova, T.V. (1961) The elastic properties of rock forming minerals, pyroxenes and amphiboles. *Bulletin of Academy of Sciences, USSR, Geophysical Series*, 871–875.
- Angel, R.J., Downs, R.T., and Finger, L.W. (2000) High-temperature–high-pressure diffraction. In R.M. Hazen and R.T. Downs, Eds., *High-Temperature and High-Pressure Crystal Chemistry*, 41, p. 559–596. Reviews in Mineralogy and Geochemistry, Mineralogical Society of America, Chantilly, Virginia.
- Arlt, T. and Angel, R.J. (2000) Displacive phase transitions in C-centred clinopyroxenes: Spodumene,  $LiScSi_2O_6$  and  $ZnSiO_3$ . *Physics and Chemistry of Minerals*, 27, 719–731.
- Arlt, T., Angel, R.J., Miletich, R., Armbruster, T., and Peters, T. (1998) High-pressure  $P2_1/c$ - $C2/c$  phase transitions in clinopyroxenes: Influences of cation size and electronic structure. *American Mineralogist*, 83, 1176–1181.
- Bindi, L., Downs, R.T., Harlow G.E., Safonov, O.G., Litvin, Y.A., Perchuk, L.L., Uchida, H., and Menchetti, S. (2006) Compressibility of synthetic potassium-rich clinopyroxene: In-situ high-pressure single-crystal X-ray study. *American Mineralogist*, 91, 802–808.
- Burnham, C.W., Clark, J.R., Papike, J.J., and Prewitt, C.T. (1967) A proposed crystallographic nomenclature for clinopyroxene structures. *Zeitschrift für*

- Kristallographie, 125, 109–119.
- Chopelas, A. and Serghiou, G. (2002) Spectroscopic evidence for pressure-induced phase transitions in diopside. *Physics and Chemistry of Minerals*, 29, 403–408.
- Downs, R.T. (2003) Topology of the pyroxenes as a function of temperature, pressure and composition determined from the procrystal electron density. *American Mineralogist*, 88, 556–566.
- Downs, R.T., Gibbs, G.V., and Boisen, M.B., Jr. (1999) Topological analysis of the  $P2_1/c$  to  $C2/c$  transition in pyroxenes as a function of temperature and pressure. *EOS Transactions, AGU, Fall Meeting Supplement*, 80 (46), F1140.
- Duffy, T.S. and Wang, Y. (1998) Pressure-volume-temperature equations of state. In R.J. Hemley, Ed., *Ultrahigh-Pressure Mineralogy, Physics and Chemistry of the Earth's Deep Interior*, 37, p. 425–457. Reviews in Mineralogy and Geochemistry, Mineralogical Society of America, Chantilly, Virginia.
- Finger, L.W. and Prince, E. (1975) A system of Fortran IV computer programs for crystal structure computations. U.S. Bureau of National Standards, Technical Note 854, 128 p.
- Gatta, G.D., Ballaran, T.B., and Iezzi, G. (2005) High-pressure X-ray and Raman study of a ferrian magnesians spodumene. *Physics and Chemistry of Minerals*, 32, 132–139.
- Hattori, T., Nagai, T., Yamanaka, T., Werner, S., and Schulz, H. (2000) Single-crystal X-ray diffraction study of  $\text{FeGeO}_3$  high- $P$  clinopyroxene ( $C2/c$ ) up to 8.2 GPa. *American Mineralogist*, 85, 1485–1491.
- Hazen, R.M. and Finger, L.W. (1977) Compressibility and crystal structure of Angra dos Reis fassaite to 52 kbar. *Annual Report of the Director, Geophysical Lab*, 1976–1977, 512–515.
- (1982) *Comparative Crystal Chemistry*, 231 p. John Wiley and Sons, New York.
- Hazen, R.M., Downs, R.T., and Prewitt, C.T. (2000) Principles of comparative crystal chemistry. In R.M. Hazen and R.T. Downs, Eds., *High-temperature and high-pressure crystal chemistry*, 41, p. 1–34. Reviews in Mineralogy and Geochemistry, Mineralogical Society of America, Chantilly, Virginia.
- Hugh-Jones, D.A. and Angel, R.J. (1994) A compressional study of  $\text{MgSiO}_3$  orthoenstatite up to 8.5 GPa. *American Mineralogist*, 79, 405–410.
- Hugh-Jones, D., Woodland, A., and Angel, R. (1994) The structure of high-pressure  $C2/c$  ferrosilite and crystal chemistry of high-pressure  $C2/c$  pyroxenes. *American Mineralogist*, 79, 1032–1041.
- Hugh-Jones, D.A., Chopelas, A., and Angel, R.J. (1997) Tetrahedral compression in  $(\text{Mg,Fe})\text{SiO}_3$  pyroxenes. *Physics and Chemistry of Minerals*, 24, 301–310.
- Ibers, J.A. and Hamilton, W.C. (1974) *International Tables for X-ray Crystallography*, IV, 366 p. Kynoch, Birmingham, U.K.
- King, H.E. and Finger, L.W. (1979) Diffracted beam crystal centering and its application to high-pressure crystallography. *Journal of Applied Crystallography*, 12, 374–378.
- Levien, L. and Prewitt, C.T. (1981) High-pressure structural study of diopside. *American Mineralogist*, 66, 315–323.
- Levien, L., Weidner, D.J., and Prewitt, C.T. (1979) Elasticity of diopside. *Physics and Chemistry of Minerals*, 4, 105–113.
- Mao, H.K., Bell, P.M., Shaner, J.W., and Steinberg, D.J. (1978) Specific volume measurements of Cu, Mo, Pd, and Ag and the calibration of the ruby R1 fluorescence pressure gauge from 0.06 to 1 Mbar. *Journal of Applied Physics*, 49, 3276–3283.
- McCarthy, A.C., Downs, R.T., and Thompson, R.M. (2008) Compressibility trends of the clinopyroxenes, and in-situ high-pressure single-crystal X-ray diffraction study of jadeite. *American Mineralogist*, 93, 198–209.
- Megaw, H. (1973) *Crystal structures: A working approach*, 249 p. Saunders, Philadelphia.
- Nestola, F., Tribaudino, M., and Boffa Ballaran, T. (2004) High pressure behavior, transformation and crystal structure of synthetic iron-free pigeonite. *American Mineralogist*, 89, 189–196.
- Nestola, F., Gatta, G.D., and Boffa Ballaran, T. (2006) The effect of Ca substitution on the elastic and structural behavior of orthoenstatite. *American Mineralogist*, 91, 809–815.
- Origlieri, M.J., Downs, R.T., Thompson, R.M., Pommier, C.J.S., Denton, M.B., and Harlow, G.E. (2003) High-pressure crystal structure study of kosmochlor,  $\text{NaCrSi}_2\text{O}_6$ , and systematics of anisotropic compression in pyroxenes. *American Mineralogist*, 88, 1025–1032.
- Pommier, C.J.S., Denton, M.B., and Downs, R.T. (2003) Raman spectroscopic study of spodumene ( $\text{LiAlSi}_2\text{O}_6$ ) through the pressure-induced change from  $C2/c$  to  $P2_1/c$ . *Journal of Raman Spectroscopy*, 34, 769–775.
- Pommier, C.J.S., Downs, R.T., Stimpfl, M., Redhammer, G.J., and Denton, M.B. (2005) Raman and X-ray investigations of  $\text{LiFeSi}_2\text{O}_6$  under pressure. *Journal of Raman Spectroscopy*, 36, 864–871.
- Press, W.H., Teukolsky, S.A., Vetterling, W.T., and Flannery, B.P. (1992) *Numerical Recipes in Fortran*, 963 p. Cambridge University Press, U.K.
- Robinson, K., Gibbs, G.V., and Ribbe, P.H. (1971) Quadratic elongation: A quantitative measure of distortion in coordination polyhedra. *Science*, 172, 567–570.
- Shannon, R.D. (1976) Revised effective ionic radii and systematic studies of interatomic distances in halides and chalcogenides. *Acta Crystallographica*, A32, 751–767.
- Thompson, R.M. and Downs, R.T. (2001) Quantifying distortion from ideal closest-packing in a crystal structure with analysis and application. *Acta Crystallographica*, B57, 119–127.
- (2002) Model Pyroxenes and Transition Pathways. 18<sup>th</sup> General Meeting of the International Mineralogical Association, 1–6 Sept, 2002, Edinburgh, Scotland. Program with Abstracts, p. 85.
- (2004) Model pyroxenes II: Structural variation as a function of tetrahedral rotation. *American Mineralogist*, 89, 614–628.
- Thompson, R.M., Downs, R.T., and Redhammer, G.T. (2005) Model pyroxenes III: Volume of  $C2/c$  pyroxenes at mantle  $P$ ,  $T$ , and  $x$ . *American Mineralogist*, 90, 1840–1851.
- Tribaudino, M., Principe, M., Bruno, M., and Levy, D. (2000) High-pressure behavior of Ca-rich  $C2/c$  clinopyroxenes along the join diopside-enstatite ( $\text{CaMgSi}_2\text{O}_6$ - $\text{Mg}_2\text{Si}_2\text{O}_6$ ). *Physics and Chemistry of Minerals*, 27, 656–664.
- Yang, H. and Prewitt, C.T. (2000) Chain and layer silicates at high temperatures and pressures. In R.M. Hazen and R.T. Downs, Eds., *High-Temperature and High-Pressure Crystal Chemistry*, 41, p. 211–255. Reviews in Mineralogy and Geochemistry, Mineralogical Society of America, Chantilly, Virginia.
- Yang, H., Finger, L.W., Conrad, P.G., Prewitt, C.T., and Hazen, R.M. (1999) A new pyroxene at high pressure: Single crystal X-ray and Raman study of the  $Pbcn$ - $P2_1cn$  phase transition in protopyroxene. *American Mineralogist*, 84, 245–256.
- Zhang, L., Ahsbahs, H., Hafner, S.S., and Kutoglu, A. (1997) Single-crystal compression and crystal structure of clinopyroxene up to 10 GPa. *American Mineralogist*, 82, 245–248.

MANUSCRIPT RECEIVED APRIL 28, 2007

MANUSCRIPT ACCEPTED SEPTEMBER 26, 2007

MANUSCRIPT HANDLED BY G. DIEGO GATTA